ACS Photonics

Article

Cite This: ACS Photonics 2019, 6, 2996−3002

pubs.acs.org/journal/apchd5

Bound States in the Continuum in Fiber Bragg Gratings

Xingwei Gao,[†,‡] Bo Zhen,[§] Marin Soljačić,[∥] Hongsheng Chen,[*,†,⊥] and Chia Wei Hsu[*,‡]

[†]State Key Laboratory of Modern Optical Instrumentation, College of Information Science & Electronic Engineering, Zhejiang University, Hangzhou 310027, China

[‡]Ming Hsieh Department of Electrical and Computer Engineering, University of Southern California, Los Angeles, California 90089, United States

[§]Department of Physics and Astronomy, University of Pennsylvania, Philadelphia, Pennsylvania 19104, United States

[∥]Department of Physics, Massachusetts Institute of Technology, Cambridge, Massachusetts 02139, United States

[⊥]The Electromagnetics Academy at Zhejiang University, Zhejiang University, Hangzhou 310027, China

Supporting Information

ABSTRACT: Optical fibers typically confine light through total internal reflection or through photonic band gaps. Here, we show that light can be perfectly guided in optical fibers through a different mechanism based on bound states in the continuum (BICs). In fibers with periodic Bragg gratings, we predict bona fide BICs in pure-polarization modes as well as quasi-BICs in hybrid-polarization modes. These BICs and quasi-BICs are topologically protected and exist robustly without the need for fine structural tuning. With a coupled-wave framework that is especially accurate for gratings with small index contrasts, we analytically prove that these BICs persist even with the very small index contrasts that are common in realistic fiber Bragg gratings. The suppression of radiation loss arises from the destructive interference between a weakly radiating local mode and a strongly radiating one. This finding opens the possibility of guiding light with BICs in optical fibers and their applications in fiber sensors, filters, and high-power fiber lasers.

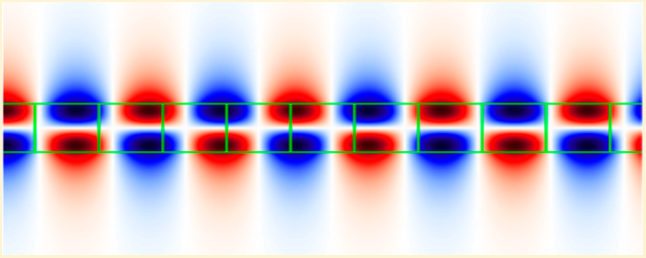

KEYWORDS: *bound states in the continuum, fiber Bragg gratings, wave coupling*

In recent years, a new paradigm for confining light emerged based on the concepts of bound states in the continuum (BICs)[1] that originated in quantum mechanics.[1−3] A BIC can achieve perfect confinement even in the presence of radiating modes in the free space. While conventional guided modes exist across a continuous range of frequencies and propagation constants, a BIC generally exists only at an isolated frequency at an isolated propagation constant.[4] Such unusual modal selectivity has many promising uses.[1] However, despite extensive research on BICs in the past few years,[1,4−14] their existence in optical fibers[15−18]—the most common medium for optical confinement—remains in doubt. Certain transverse patterning of photonic crystal fibers can significantly suppress leakage without a band gap,[19,10−21] but there exist residual radiation losses even for a perfect structure. Fibers with separable transverse permittivity profiles have been suggested for fiber BICs,[22] but they require exact permittivity values that cannot be realized in practice. Therefore, the large optical-fiber community has not been able to reap the benefits of BICs.

Certain periodic structures are known to exhibit BICs.[4,7,8,10−14,21,23−38] While periodic Bragg gratings in fibers can be readily realized through laser pulses or by writing interference fringes onto a photosensitive core,[39−46] the grating index contrast Δ_n is typically at 10^{-6}−10^{-2}.[39,41,44] The small index contrasts become a roadblock as conventional simulation methods for studying BICs cannot resolve the fine differences in quality factor for modes in such low-contrast structures.

Here, we show, for the first time, that bona fide BICs exist in optical fibers with Bragg gratings, despite the vanishingly small index contrasts. With customized numerical simulations and an analytical coupled-wave analysis, we show that these BICs exist robustly without fine structural tuning or index tuning, and that they persist when the index contrast goes down. In addition, we also find quasi-BICs where the radiation loss can be suppressed by orders of magnitude. Our results indicate that BICs readily exist in a wide range of fiber Bragg grating structures, with great promise for experimental realizations and new applications.

RIGOROUS COUPLED-WAVE ANALYSIS FORMALISM

We consider a step-index fiber with periodic index modulations in the core [Figure 1a]. The core has radius r and is surrounded by a cladding with relative permittivity ε_d. The index modulation has periodicity a. For concreteness, we consider the modulation to consist of alternating dielectric

Received: August 20, 2019
Published: October 16, 2019

DOI: 10.1021/acsphotonics.9b01202
ACS Photonics 2019, 6, 2996−3002

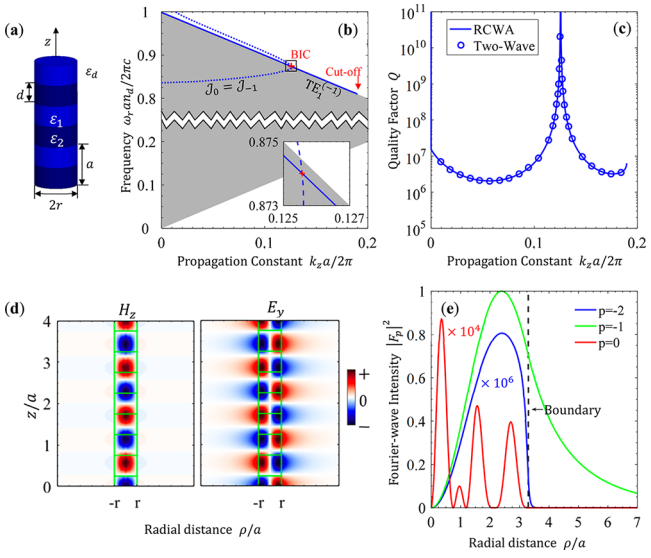

Figure 1. Bound state in the continuum (BIC) in fiber Bragg gratings. (a) Schematic of a fiber Bragg grating considered here. The fiber core is cylindrically symmetric, periodic in the z direction with periodicity a, and surrounded by a cladding with relative permittivity ε_d. (b) Band structure and (c) quality factor of the $TE_1^{(-1)}$ eigenmode. The cladding has index $n_d = 1.444$. The core has index $\sqrt{\varepsilon_1} = 1.455$, radius $r = 3.3a$, with permittivity contrast $\Delta_\varepsilon \equiv (\varepsilon_2 - \varepsilon_1)/\varepsilon_1 = 10^{-2}$; $\Delta_n = 5 \times 10^{-3}$. The quality factor diverges at $k_z \approx 0.126(2\pi/a)$, where the leaky mode turns into a BIC. The gray shaded region in part b indicates the frequency range where there is one radiation channel in the continuum, namely, $|k_z - 2\pi/a|c/\sqrt{\varepsilon_d} > \omega_r > |k_z|c/\sqrt{\varepsilon_d}$. In this region of continuum, only −1st Fourier Component is radiative. The inset of part b shows a zoom-in close to the BIC. The blue dotted curve is the solution of $\mathcal{J}_0 = \mathcal{J}_{-1}$ described in the Two-Wave Coupling Analysis section; its intersection with the $TE_1^{(-1)}$ band is the location of the BIC, marked with a red plus. The solid curve and the circles in part c are from full RCWA solution (including 11 Fourier terms) and the two-wave approximation, respectively. (d) Mode profile and (e) intensities of the main Fourier components of the BIC. The $|F_{-2}|^2$ and $|F_0|^2$ curves are multiplied by 10^6 and 10^4 to be more visible.

layers with thicknesses d and $a - d$ at relative permittivities ε_2 and ε_1; our formalism is general and also treats other periodic profiles. The permittivity contrast is defined as $\Delta_\varepsilon \equiv (\varepsilon_2 - \varepsilon_1)/\varepsilon_1$, and the index contrast is $\Delta_n \equiv (n_2 - n_1)/n_1 \approx \Delta_\varepsilon/2$. The cladding's outer surface is not considered since the field is exponentially small there for the BICs of interest. Given the cylindrical symmetry, the fiber modes have $\exp(im\phi)$ angular dependence with distinct angular momentum indices m, where ϕ is the azimuthal angle. We start by considering fiber modes with $m = 0$, for which the TE ($\boldsymbol{H} = H_z\hat{z} + H_\rho\hat{\rho}$, $\boldsymbol{E} = E_\phi\hat{\phi}$) and TM ($\boldsymbol{E} = E_z\hat{z} + E_\rho\hat{\rho}$, $\boldsymbol{H} = H_\phi\hat{\phi}$) polarizations decouple,[17] and each mode couples only to radiation channels in one polarization. We label these pure-polarization modes as TE_n and TM_n where n is the radial mode index. The hybrid-polarization modes with $m \neq 0$ will be considered later.

The low index contrast and extremely high quality factor of the leaky fiber modes post a challenge for the often-used finite-difference or finite-element numerical methods. To accurately describe the leaky fiber modes, we employ the Fourier modal method, also called rigorous coupled-wave analysis[47,48] (RCWA); RCWA describes the radiating fields analytically, is particularly efficient when the contrast of the periodic index modulation is small, and can readily handle very large quality factors. Here, we briefly summarize the RCWA formalism and our implementation. We look for solutions of the full vectorial Maxwell's equations with an $\exp(-i\omega t)$ time dependence and satisfying an outgoing boundary condition at $\rho \to \infty$; they are called quasinormal modes[49] or simply resonances, and we will also refer to them as the eigenmodes of the fiber Bragg grating. The angular frequency ω is generally complex-valued ($\omega = \omega_r + i\omega_i$) with a negative imaginary part that corresponds to a decay in time because of radiation loss. The lifetime of the resonance is quantified by its quality factor, $Q = -\omega_r/(2\omega_i)$. Fields of the TE_n and TM_n modes inside and outside the core (where the relative permittivity ε is a function of z only) satisfy

$$\text{TE: } (\nabla^2 + k_0^2\varepsilon)H_z(\rho, z) = 0$$
$$\text{TM: } \left(\nabla^2 + k_0^2\varepsilon + \frac{\partial}{\partial z}\frac{\varepsilon'}{\varepsilon}\right)E_z = 0 \tag{1}$$

where $k_0 = \omega/c$, and c is the vacuum speed of light. Inside the core ($\rho < r$), ε is periodic with $\varepsilon(z + a) = \varepsilon(z)$. Outside the core ($\rho > r$), $\varepsilon = \varepsilon_d$ is a constant. By solving eq 1 inside and outside the core and imposing an outgoing boundary condition outside, we can write the general expression of a TE eigenmode as

$$H_z(\rho, z) = \begin{cases} e^{ik_z z}\sum_p C_p u_p(z)\dfrac{J_0(\gamma_p\rho)}{J_0(\gamma_p r)}, & \rho < r \\ e^{ik_z z}\sum_p T_p e^{i(\frac{2\pi p}{a})z}\dfrac{H_0(\kappa_p\rho)}{H_0(\kappa_p r)}, & \rho > r \end{cases} \tag{2}$$

where k_z is the Bloch wave number (the axial propagation constant), and $\{u_p\}$ is a set of local modes in the core satisfying

$$\left[\left(\frac{\partial}{\partial z} + ik_z\right)^2 + k_0^2\varepsilon(z)\right]u_p(z) = \gamma_p^2 u_p(z) \tag{3}$$

and $u_p(z) = u_p(z + a)$. Here, γ_p is the radial propagation constant of the local mode inside the core, and $\kappa_p = \sqrt{\varepsilon_d k_0^2 - (k_z + 2\pi p/a)^2}$ is the radial propagation constant outside. J_0 and H_0 are the zeroth Bessel function and Hankel function of the first kind. As the operator on the left-hand side of eq 3 is Hermitian, γ_p^2 is real, and $\{u_p\}$ and $\{\exp(i2\pi pz/a)\}$ each forms a complete basis for functions periodic in z. We index the local modes, $p = 0, \pm1, \pm2, \ldots$, by the primary Fourier component of u_p. The coefficients C_p and T_p are to be chosen to satisfy continuity across the core-cladding interface. Taking a real-valued propagation constant k_z, we numerically solve eq 3 in the Fourier basis for u_p and γ_p^2 and then impose continuity of H_z and E_ϕ at $\rho = r$ via eq 2 to obtain the complex frequency $\omega = \omega_r + i\omega_i$ of the eigenmode and its field profile. In the following, we label the resulting TE modes as $TE_n^{(q)}$, where q is the main Fourier component, and n is the radial index. The same method works for TM modes by working with E_z in eq 1. The only approximation of this method is a truncation of terms in the Fourier basis, and we check that the result converges rapidly with an increasing number of terms. This method remains robust when the index contrast is small. In fact, since the different terms in the summation are coupled through the periodic index modulation, smaller contrast means weaker coupling and fewer terms to keep; we will take advantage of this property to develop a two-term approximation below.

DOI: 10.1021/acsphotonics.9b01202
ACS Photonics 2019, 6, 2996−3002

We use high-contrast gratings as a test case for our RCWA implementation; such a case is similar to the chain-of-disks structure recently studied in refs 14, 36, and 37. Figure S1 and Section I in the Supporting Information compare results from our RCWA implementation with those from a commercial finite-element frequency-domain software for the case $\varepsilon_2 = 2.16$, $\varepsilon_1 = \varepsilon_d = 1$; the perfect agreement indicates that our implementation is valid.

Note that, instead of looking for complex-frequency solutions at real propagation constants k_z, one can also look for complex-k_z solutions at real frequencies. We show in Section II and Figure S2 in the Supporting Information that, for the high-Q modes of interest here, these two approaches are equivalent under a simple conversion.

BOUND STATES IN THE CONTINUUM IN FIBER BRAGG GRATINGS

We now consider a realistic fiber Bragg grating with a grating contrast of $\Delta_\varepsilon = 10^{-2}$ ($\Delta_n = 5 \times 10^{-3}$). The fiber parameters are chosen to be comparable to those of a commercial fiber (Fibercore SM1500P). Here, we examine the $TE_1^{(-1)}$ band, whose dispersion calculated from RCWA is shown in Figure 1b. At frequencies above the light line, $\omega_r > |k_z|c/\sqrt{\varepsilon_d}$, the eigenmodes couple to the continuum of free-space modes in the cladding and are generally leaky with finite quality factors. However, we find that the quality factor diverges to infinity at a discrete propagation constant $k_z \approx 0.126 \times 2\pi/a$, where the leaky resonance turns into a lossless BIC [Figure 1c]. The field profile of the BIC [Figure 1d] exhibits exponential decay outside the fiber core, with no outward propagation.

The disappearance of radiation can be quantified by the Fourier components $F_p(\rho)$ of the field profile, defined via $E_\Phi(\rho, z) = e^{ik_z z}\sum_p [F_p(\rho)\exp(i2\pi pz/a)]$ and shown in Figure 1e. The zeroth Fourier component F_0 is the one that carries outgoing radiation into the cladding. For this BIC, we observe that F_0 is nonzero inside the fiber core, indicating that there are interior fields that cannot be confined by total internal reflection. However, F_0 vanishes outside the core and thus does not carry outgoing radiation. This disappearance of radiation results because, at the core-cladding interface ($\rho = r$), multiple local modes u_p in the fiber core destructively interfere to completely cancel the zeroth Fourier component, as we can see more clearly in the next section.

We note that BICs may also arise through separability due to symmetry[1] as can be seen at $k_z = 0$ in Figure 1c; more details are given in Figure S3. For such BICs, F_0 is zero both inside and outside the fiber core because of symmetry. These symmetry-protected BICs have zero group velocity and do not propagate along the fiber.

TWO-WAVE COUPLING ANALYSIS

The low grating contrast suggests that we can understand the leaky resonance and the BIC based on modes of a homogeneous fiber without grating. The dispersion of the TE modes for a homogeneous fiber is given by[17]

$$\frac{J_0'(\gamma_{0,p}r)}{\gamma_{0,p}J_0(\gamma_{0,p}r)} = \frac{H_0'(\kappa_p r)}{\kappa_p H_0(\kappa_p r)} \tag{4}$$

where $\gamma_{0,p} = \sqrt{k_0^2\varepsilon_c - (k_z + 2\pi p/a)^2}$, and ε_c is the relative permittivity of the core. The solutions of eq 4 are plotted in Figure 2a,b. Here, the Fourier index p of each band $TE_n^{(p)}$ corresponds to band folding in the reduced-zone scheme as we impose an artificial periodicity a. In this homogeneous case, each band contains a single Fourier component with $\mu_p(z) = e^{i(2\pi p/a)z}$, and there is no coupling between bands. Fiber modes with frequency above the unfolded light line ($\omega_r > |k_z + 2\pi p/a|c/\sqrt{\varepsilon_d}$) are leaky and radiate strongly, as can be seen from their Q factors [Figure 2b]. Those below the unfolded light line are index guided and do not radiate. In Figure 2 we illustrate using a fiber without cladding ($\varepsilon_d = 1$) and with periodicity $a = r$ so that the relevant fiber modes are easier to see in the band structure.

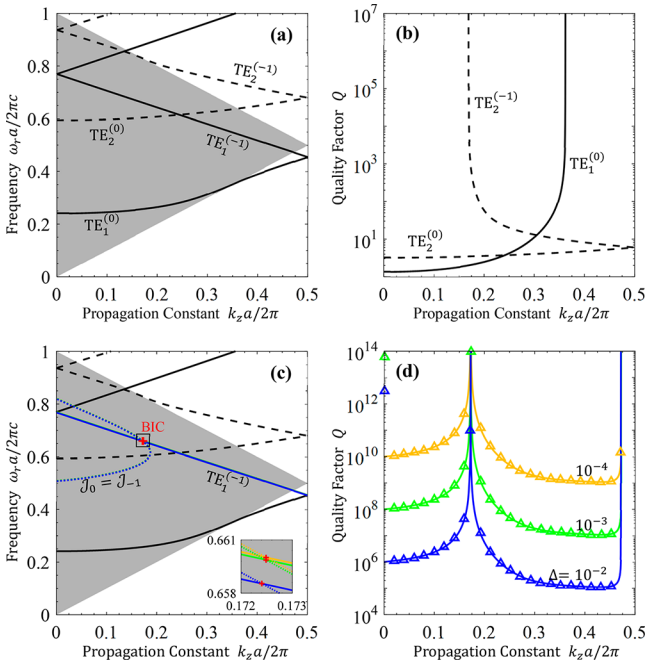

Figure 2. Illustration of the two-wave coupling analysis. (a, b) Modes of a homogeneous fiber with dielectric $\varepsilon_1 = \varepsilon_2 \equiv \varepsilon_c = 2.12$ in $\varepsilon_d = 1$. (a) Band structure of the TE modes with $m = 0$. By artificially setting a period of $a = r$ along the z direction, the dispersion curves are folded into the Brillouin zone. Solid and dashed curves are $TE_1^{(q)}$ and $TE_2^{(q)}$ modes with different Fourier indices q. The gray shaded area marks the radiation continuum with one leaky channel. (b) Quality factor Q of the leaky fiber modes. The $TE_1^{(-1)}$ band is not shown as it has infinite Q in the homogeneous fiber. (c, d) Dispersion curves in the presence of a low-contrast grating, which couples the $TE_z^{(0)}$ and $TE_1^{(-1)}$ bands. (c) Band structure and (d) quality factors of the $TE_1^{(-1)}$ eigenmodes. The blue, green, and orange solid curves are two-wave approximations with the grating permittivity contrast Δ_ε being 10^{-2}, 10^{-3}, and 10^{-4}, respectively, and the colored triangles are full RCWA solutions including 11 Fourier orders. The inset of part c is a zoom-in close to the BICs, and the dotted curves are the solutions of $\mathcal{J}_0 = \mathcal{J}_{-1}$.

The periodic index modulation couples the different Fourier components. Modes above the light line that were guided in the homogeneous fiber can now radiate by coupling to the leaky modes with $p = 0$, analogous to the guided resonances in photonic crystal slabs.[50] Because of the low index modulation, the dominant Fourier component F_{-1} of the $TE_1^{(-1)}$ band only couples appreciably to the neighboring components F_0 and F_{-2}; the other components are orders of magnitude smaller. Among these three central components, F_{-2} has the smallest weight [as shown in Figure 1e] and does not contribute to radiation. Away from the other bands (which may carry other Fourier components), there are no other components in

DOI: 10.1021/acsphotonics.9b01202
ACS Photonics 2019, 6, 2996−3002

$\mathrm{TE}_1^{(-1)}$. Therefore, we expect that a two-wave approximation, keeping only the F_0 and F_{-1} components in RCWA, will suffice in describing the leaky resonances and the propagating BICs of interest.

When only the F_0 and F_{-1} Fourier components are kept, the eigenmode's continuity of H_z and E_ϕ at the core-cladding interface ($\rho = r$) is expressed as (see Section III in the Supporting Information for derivation)

$$\begin{bmatrix} 1 & \sigma \\ -\sigma & 1 \end{bmatrix} \begin{bmatrix} C_0 \\ C_{-1} \end{bmatrix} = \begin{bmatrix} T_0 \\ T_{-1} \end{bmatrix} \tag{5}$$

$$\begin{bmatrix} 1 & \sigma \\ -\sigma & 1 \end{bmatrix} \begin{bmatrix} \mathcal{J}_0 & 0 \\ 0 & \mathcal{J}_{-1} \end{bmatrix} \begin{bmatrix} C_0 \\ C_{-1} \end{bmatrix} = \begin{bmatrix} \mathcal{H}_0 & 0 \\ 0 & \mathcal{H}_{-1} \end{bmatrix} \begin{bmatrix} T_0 \\ T_{-1} \end{bmatrix} \tag{6}$$

where $\mathcal{J}_p \triangleq J_0'(\gamma_p r)/[\gamma_p J_0(\gamma_p r)]$ and $\mathcal{H}_p \triangleq H_0'(\kappa_p r)/[\kappa_p H_0(\kappa_p r)]$. The dimensionless coefficient $\sigma \triangleq k_0^2 \varepsilon_\Delta/({\gamma_{0,-1}}^2 - {\gamma_{0,0}}^2)$ couples the two bands $\mathrm{TE}_n^{(0)}$ and $\mathrm{TE}_{n'}^{(-1)}$, with ε_Δ being the first-order Fourier coefficient of the core index profile $\varepsilon(z)$; for the alternating-index grating here, $\varepsilon_\Delta = \varepsilon_1 \Delta(d/a)\ \mathrm{sinc}(d/a)$. Away from the Brillouin zone edge, ${\gamma_0}^2 \approx {\gamma_{0,0}}^2 - \sigma k_0^2 \varepsilon_\Delta$, ${\gamma_{-1}}^2 \approx {\gamma_{0,-1}}^2 + \sigma k_0^2 \varepsilon_\Delta$.

Combining eqs 5 and 6, we find that nonzero solutions exist when

$$(\mathcal{J}_0 - \mathcal{H}_0)(\mathcal{J}_{-1} - \mathcal{H}_{-1}) + (\mathcal{J}_0 - \mathcal{H}_{-1})(\mathcal{J}_{-1} - \mathcal{H}_0)\sigma^2 = 0 \tag{7}$$

which is the dispersion relation that yields the complex-valued frequencies of the eigenmodes on the $\mathrm{TE}_n^{(0)}$ and $\mathrm{TE}_{n'}^{(-1)}$ bands. When $\sigma \to 0$, eq 7 reduces to eq 4. Figure 2c,d shows the $\mathrm{TE}_1^{(-1)}$ solution of eq 7 for three different grating permittivity contrasts ($\Delta_\varepsilon = 10^{-2}, 10^{-3}, 10^{-4}$) in blue, green, and orange solid curves, which agree quantitatively with the full RCWA solutions (shown in triangles). Discrepancy can only be observed very close to $k_z = 0$, where the $\mathrm{TE}_1^{(-1)}$ band hybridizes with the $\mathrm{TE}_1^{(1)}$ band and acquires an additional F_1 Fourier component. The corresponding solution for the example in Figure 1 is plotted as blue circles in Figure 1c, again showing excellent agreement.

This two-wave coupling analysis also clarifies how the local modes in the fiber core interfere to suppress radiation in the combined eigenmode. In particular, eqs 5 and 6 show that the radiation amplitude T_0 is given by $T_0 = C_0 + \sigma C_{-1}$ or $\mathcal{H}_0 T_0 = \mathcal{J}_0 C_0 + \sigma \mathcal{J}_{-1} C_{-1}$ (from H_Z and E_ϕ, respectively). In both expressions, the two terms on the right-hand side are the two constituent local modes of the fiber core evaluated at the core-cladding interface. While neither term is zero, the superposition of the two terms can be small or even zero through destructive interference. Figure S3 in the Supporting Information further illustrates this concept with a decomposition of the field profile. Destructive interference is also the cause of BICs in the coupled-resonances model of Friedrich and Wintgen.[1,3,51−55] We emphasize, however, that we did not adapt the Friedrich−Wintgen model here; we solve the full vectorial Maxwell's equations, and the only approximation made is a controlled truncation of Fourier terms.

The two-wave coupling analysis also yields a simple analytical prediction for the locations of the BICs. Equations 5 and 6 show that $T_0/C_0 = (\mathcal{J}_{-1} - \mathcal{J}_0)/(\mathcal{J}_{-1} - \mathcal{H}_0)$ for an eigenmode. Therefore, the above-mentioned destructive interference can completely suppress radiation ($T_0 = 0$) and lead to a BIC when $\mathcal{J}_{-1} = \mathcal{J}_0$ and $\mathcal{J}_{-1} \neq \mathcal{H}_0$. Inserting this condition into eq 7, we find that a BIC is the simultaneous solution of two equations:

$$\mathcal{J}_0 = \mathcal{J}_{-1},\ \ \mathcal{J}_{-1} = \mathcal{H}_{-1} \tag{8}$$

Importantly, note that both equations have solutions at real-valued frequencies; the second one $\mathcal{J}_{-1} = \mathcal{H}_{-1}$ is essentially the homogeneous-fiber dispersion [eq 4 except for a minor difference between γ_{-1} and $\gamma_{0,-1}$ that is negligible at low contrast]. Therefore, the two sets of solution curves can intersect at real-valued frequencies corresponding to the BICs. The solution of $\mathcal{J}_0 = \mathcal{J}_{-1}$ is plotted in blue dashed curves in Figures 1b and 2c. Indeed, its intersection with the homogeneous-fiber dispersion gives the BICs marked by red pluses.

Being at the intersection of two curves, the BIC is robust under small parameter changes of the system (which will only shift the curves). This is an example of a 1D topological defect (with one radiation amplitude that crosses zero), analogous to the 2D topological defects in systems with two radiation channels.[10,12,28,31,32]

The topological protection is powerful but does not tell us whether a BIC can persist in the vanishing-contrast limit, since a BIC can disappear by annihilating with another BIC or by moving underneath the light line. However, here we know that the BICs of interest do persist in such limit: for vanishingly small index contrasts ($\Delta_\varepsilon \to 0$, $\gamma_p \to \gamma_{0,p}$), the solutions of eq 8 approach a set of fixed points, as can be seen in Figure 2c. Therefore, we now have an analytic proof that, for small index contrasts, the BICs approach fixed locations in the band structure and do not vanish.

TIME-DOMAIN SIMULATIONS

In time domain, the suppression of radiation manifests as an absence of decay with time after the mode is excited by near-field sources. Here, we explicitly show such temporal responses using finite-difference time-domain (FDTD) simulations.[56,57] Ring sources with frequency ω_r and Bloch wavenumber k_z of the modes of interest are placed in each unit cell of the grating. We turn off the sources at time t_0 and continue to observe the evolution of field intensity at a location inside the fiber core. Figure 3 shows the result for three modes on the $\mathrm{TE}_1^{(-1)}$ band

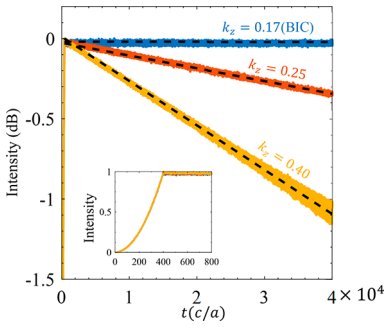

Figure 3. Temporal responses of $\mathrm{TE}_1^{(-1)}$ modes under a step-source excitation. Inset shows the short-time evolution of the normalized intensity in linear scale; the source is switched off at $t = t_0 = 400(a/c)$. The main plot shows the long-time evolution of the intensity in dB. Black dashed lines are predictions $\exp(2\omega_i t)$ from the two-wave coupling theory. The system is the same as the $\Delta_\varepsilon = 10^{-2}$ case in Figure 2c.

DOI: 10.1021/acsphotonics.9b01202
ACS Photonics 2019, 6, 2996−3002

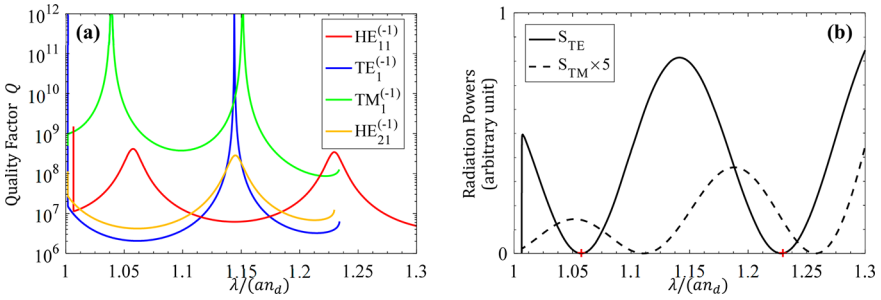

Figure 4. (a) RCWA result of the quality factors of the first few eigenmodes for the fiber Bragg grating considered in Figure 1, as a function of the normalized wavelength $\lambda = 2\pi c/\omega_r$. (b) Two radiation strengths of the $HE_{11}^{(-1)}$ mode. Red crosses indicate the peaks of $HE_{11}^{(-1)}$'s quality factor. The TM-polarized radiation strength S_{TM} is multiplied by 5 to be more visible.

with different k_z from the $\Delta_\varepsilon = 10^{-2}$ case in Figure 2c,d. The two finite-Q resonances decay exponentially with time after the source is turned off. Meanwhile, no attenuation is visible for the mode at the expected location of the BIC, $k_z = 0.17 \times (2\pi/a)$ and $\omega_r = 0.66 \times (2\pi c/a)$. In Figure 3b, we superimpose the expected time dependences $\exp(2\omega_i t)$ with ω_i from the preceding two-wave approximation; they fully agree with the time-domain simulation results.

HYBRID-POLARIZATION EIGENMODES AND QUASI-BICS

Having established the existence of BICs in the TE eigenmodes, we now extend our analysis to modes of the other polarizations. For the TM modes with $m = 0$ (for which $\boldsymbol{E} = E_z\hat{z} + E_\rho\hat{\rho}$, $\boldsymbol{H} = H_\phi\hat{\phi}$), E_z in the cladding ($\rho > r$) is expressed as $E_z = e^{ik_z z}\sum_p T_{p,TM} e^{i(2\pi p/a)z} H_0(\kappa_p\rho)/H_0(\kappa_p r)$, similar to H_z in eq 2. When the angular momentum index m is nonzero, the two polarizations are coupled, and there are two sets of radiation channels characterized by $T_{p,TM}$ and $T_{p,TE}$. For $HE_{11}^{(-1)}$ here, the relative radiation strengths are $S_{TE} = \mu_0|T_{0,TE}|^2/(\varepsilon_0 n_d^2)$ and $S_{TM} = |T_{0,TM}|^2$ (see Section IV in the Supporting Information). The quality factors of the first few bands of eigenmodes, including $TE_1^{(-1)}$, $TM_1^{(-1)}$, $HE_{21}^{(-1)}$, and the fundamental mode $HE_{11}^{(-1)}$, are shown in Figure 4a for the structure considered in Figure 1. Note that even though $TE_1^{(-1)}$, $TM_1^{(-1)}$, and $HE_{21}^{(-1)}$ are degenerate in the absence of the grating (together they make up the LP11 group[17]), they take on different radiation losses when the grating is introduced. In the $TM_1^{(-1)}$ band, two BICs can be readily identified; the mechanism is the same as the BICs in $TE_1^{(-1)}$ since there is only one radiation channel. The sharp variation of the quality factor near $k_z = 0$ (wavelength $\lambda \approx an_d$) is further detailed in Figure S4.

The hybrid-polarization eigenmodes $HE_{11}^{(-1)}$ and $HE_{21}^{(-1)}$ couple to two radiation channels (in TE and TM polarizations). As shown in Figure 4b for the $HE_{11}^{(-1)}$ mode, each of the two radiation powers S_{TE} and S_{TM} crosses zero at discrete frequencies and propagation constants. Generically they vanish at different points, so there is no bona fide BIC in these hybrid-polarization eigenmodes. However, since $T_{0,TE}$ is the dominant radiation channel, the quality factor reaches local maxima near the zeros of $T_{0,TE}$, forming quasi-BICs where the quality factor is enhanced by almost 2 orders of magnitude. Despite the finite quality factors, such quasi-BICs can also be very useful for applications.[1,19−21,55,58−60]

CONCLUSION AND DISCUSSION

We have shown that BICs and quasi-BICs exist in realistic fiber Bragg gratings with low index-modulation contrasts. An analytical proof was provided through a two-wave coupling analysis we developed. The BICs arise from the coupling between a high-Q-band and a low-Q-band, and they persist in the limit of vanishingly small index contrasts.

Such fiber BICs and quasi-BICs have distinct properties that can enable new avenues of applications. While a fiber Bragg grating operating near the Bragg wavelength exhibits narrowband reflection, one that operates near the BIC or quasi-BIC wavelength exhibits narrowband transmission instead. As such, the BICs and quasi-BICs can naturally serve as in-line bandpass filters. The BIC wavelength and quality factor depend on environmental factors, which can be tailored and optimized for different remote sensing applications. The unique modal selectivity of BICs and quasi-BICs can be used as a Q-spoiling mechanism for the single-mode operation of fiber lasers. The wide availability of optical fibers and the ease of writing Bragg gratings on them will ease experimental realizations and facilitate such applications.

ASSOCIATED CONTENT

Supporting Information

The Supporting Information is available free of charge on the ACS Publications website at DOI: 10.1021/acsphotonics.9b01202.

Fiber Bragg gratings with large index modulation, complex-ω modes versus complex-k_z modes, two-wave coupling analysis for TE modes, and hybrid modes in fiber Bragg gratings (PDF)

AUTHOR INFORMATION

Corresponding Authors

*E-mail: hansomchen@zju.edu.cn.
*E-mail: cwhsu@usc.edu.

ORCID

Xingwei Gao: 0000-0001-8160-7426
Hongsheng Chen: 0000-0002-5735-9781

Notes

The authors declare no competing financial interest.

ACKNOWLEDGMENTS

X.G. and H.C. were supported by the Interdisciplinary Center for Quantum Information, State Key Laboratory of Modern Optical Instrumentation, College of Information Science and Electronic Engineering, Zhejiang University, Hangzhou

DOI: 10.1021/acsphotonics.9b01202
ACS Photonics 2019, 6, 2996−3002

310027, China. C.W.H. was supported by the National Science Foundation through Grant DMR-1307632. B.Z. was supported by the Air Force Office of Scientific Research under Award FA9550-18-1-0133. M.S. was supported by the MRSEC Program of the National Science Foundation under Award DMR-1419807 and the Army Research Office under Cooperative Agreement W911NF-18-2-0048.

REFERENCES

(1) Hsu, C. W.; et al. Bound states in the continuum. *Nature Reviews Materials* **2016**, *1*, 16048.
(2) Von Neumann, J.; Wigner, E. Uber merkwürdige diskrete Eigenwerte. Uber das Verhalten von Eigenwerten bei adiabatischen Prozessen. *Physikalische Zeitschrift* **1929**, *30*, 465−467.
(3) Friedrich, H.; Wintgen, D. Interfering resonances and bound states in the continuum. *Phys. Rev. A: At., Mol., Opt. Phys.* **1985**, *32* (6), 3231.
(4) Hsu, C. W.; et al. Observation of trapped light within the radiation continuum. *Nature* **2013**, *499* (7457), 188−91.
(5) Corrielli, G.; et al. Observation of Surface States with Algebraic Localization. *Phys. Rev. Lett.* **2013**, *111* (22), 220403.
(6) Weimann, S.; et al. Compact Surface Fano States Embedded in the Continuum of Waveguide Arrays. *Phys. Rev. Lett.* **2013**, *111* (24), 240403.
(7) Gansch, R.; et al. Measurement of bound states in the continuum by a detector embedded in a photonic crystal. *Light: Sci. Appl.* **2016**, *5* (9), No. e16147.
(8) Kodigala, A.; et al. Lasing action from photonic bound states in continuum. *Nature* **2017**, *541* (7636), 196−199.
(9) Gomis-Bresco, J.; Artigas, D.; Torner, L. Anisotropy-induced photonic bound states in the continuum. *Nat. Photonics* **2017**, *11* (4), 232−236.
(10) Zhang, Y.; et al. Observation of Polarization Vortices in Momentum Space. *Phys. Rev. Lett.* **2018**, *120* (18), 186103.
(11) Zhang, W.; et al. Extraordinary optical reflection resonances and bound states in the continuum from a periodic array of thin metal plates. *Opt. Express* **2018**, *26* (10), 13195−13204.
(12) Doeleman, H. M.; et al. Experimental observation of a polarization vortex at an optical bound state in the continuum. *Nat. Photonics* **2018**, *12* (7), 397−401.
(13) Bahari, B. et al. *Integrated and Steerable Vortex Lasers using Bound States in Continuum*; Bulletin of the American Physical Society, 2018.
(14) Sadrieva, Z. F.; et al. Experimental observation of a symmetry-protected bound state in the continuum in a chain of dielectric disks. *Phys. Rev. A: At., Mol., Opt. Phys.* **2019**, *99* (5), 053804.
(15) Lee, B. Review of the present status of optical fiber sensors. *Opt. Fiber Technol.* **2003**, *9* (2), 57−79.
(16) Russell, P. Photonic Crystal Fibers. *Science* **2003**, *299* (5605), 358−362.
(17) Agrawal, G. P. *Fiber-optic communication systems*; John Wiley & Sons, 2012; Vol. *222*.
(18) Zervas, M. N.; Codemard, C. A. High Power Fiber Lasers: A Review. *IEEE J. Sel. Top. Quantum Electron.* **2014**, *20* (5), 219−241.
(19) Couny, F.; et al. Generation and Photonic Guidance of Multi-Octave Optical-Frequency Combs. *Science* **2007**, *318* (5853), 1118−1121.
(20) Debord, B.; et al. Ultralow transmission loss in inhibited-coupling guiding hollow fibers. *Optica* **2017**, *4* (2), 209−217.
(21) Bulgakov, E.; Sadreev, A. Fibers based on propagating bound states in the continuum. *Phys. Rev. B: Condens. Matter Mater. Phys.* **2018**, *98* (8), 085301.
(22) Birks, T. A. et al. In *Strictly-bound modes of an idealised hollow-core fibre without a photonic bandgap*, 36th European Conference and Exhibition on Optical Communication, 2010.
(23) Shipman, S. P.; Venakides, S. Resonance and Bound States in Photonic Crystal Slabs. *SIAM J. Appl. Math.* **2003**, *64* (1), 322−342.
(24) Marinica, D. C.; Borisov, A. G.; Shabanov, S. V. Bound States in the continuum in photonics. *Phys. Rev. Lett.* **2008**, *100* (18), 183902.
(25) Liu, V.; Povinelli, M.; Fan, S. Resonance-enhanced optical forces between coupled photonic crystal slabs. *Opt. Express* **2009**, *17* (24), 21897−21909.
(26) Hsu, C. W.; et al. Bloch surface eigenstates within the radiation continuum. *Light: Sci. Appl.* **2013**, *2*, No. e84.
(27) Yang, Y.; et al. Analytical perspective for bound states in the continuum in photonic crystal slabs. *Phys. Rev. Lett.* **2014**, *113* (3), 037401.
(28) Zhen, B.; et al. Topological Nature of Optical Bound States in the Continuum. *Phys. Rev. Lett.* **2014**, *113* (25), 257401.
(29) Bulgakov, E. N.; Sadreev, A.F. Light trapping above the light cone in one-dimensional array of dielectric spheres. *Phys. Rev. A: At., Mol., Opt. Phys.* **2015**, *92* (2), 023816.
(30) Gao, X. Formation mechanism of guided resonances and bound states in the continuum in photonic crystal slabs. *Sci. Rep.* **2016**, *6*, 31908.
(31) Bulgakov, E. N.; Maksimov, D. N. Topological Bound States in the Continuum in Arrays of Dielectric Spheres. *Phys. Rev. Lett.* **2017**, *118* (26), 267401.
(32) Bulgakov, E. N.; Maksimov, D. N. Bound states in the continuum and polarization singularities in periodic arrays of dielectric rods. *Phys. Rev. A: At., Mol., Opt. Phys.* **2017**, *96* (6), 063833.
(33) Xiao, Y.-X.; et al. Topological Subspace-Induced Bound State in the Continuum. *Phys. Rev. Lett.* **2017**, *118* (16), 166803.
(34) Yuan, L.; Lu, Y. Y. Strong resonances on periodic arrays of cylinders and optical bistability with weak incident waves. *Phys. Rev. A: At., Mol., Opt. Phys.* **2017**, *95* (2), 023834.
(35) Yuan, L.; Lu, Y. Y. Bound states in the continuum on periodic structures: perturbation theory and robustness. *Opt. Lett.* **2017**, *42* (21), 4490−4493.
(36) Bulgakov, E. N.; Sadreev, A. F. Bound states in the continuum with high orbital angular momentum in a dielectric rod with periodically modulated permittivity. *Phys. Rev. A: At., Mol., Opt. Phys.* **2017**, *96* (1), 013841.
(37) Bulgakov, E. N.; Sadreev, A. F. Scattering plane waves by a dielectric cylinder with periodically modulated permittivity at oblique incidence. *Phys. Rev. A: At., Mol., Opt. Phys.* **2018**, *97* (6), 063856.
(38) Cerjan, A.; Hsu, C.W.; Rechtsman, M.C. Bound States in the Continuum through Environmental Design. *Phys. Rev. Lett.* **2019**, *123*, No. 023902.
(39) Russell, P. S. J.; Archambault, J.-L.; Reekie, L. Fibre gratings. *Phys. World* **1993**, *6* (10), 41.
(40) Hill, K. O.; Meltz, G. Fiber Bragg grating technology fundamentals and overview. *J. Lightwave Technol.* **1997**, *15* (8), 1263−1276.
(41) Othonos, A. Fiber Bragg gratings. *Rev. Sci. Instrum.* **1997**, *68* (12), 4309−4341.
(42) Kashyap, R. Photosensitivity and Photosensitization of Optical Fibers. In *Fiber Bragg Gratings*, 2nd ed.; Academic Press: Boston, 2010; Chapter 2, pp 15−51.
(43) Thomas, J.; et al. Femtosecond pulse written fiber gratings: a new avenue to integrated fiber technology. *Laser & Photonics Reviews* **2012**, *6* (6), 709−723.
(44) Homoelle, D.; et al. Infrared photosensitivity in silica glasses exposed to femtosecond laser pulses. *Opt. Lett.* **1999**, *24* (18), 1311−1313.
(45) Martinez, A.; et al. Direct writing of fibre Bragg gratings by femtosecond laser. *Electron. Lett.* **2004**, *40* (19), 1170−1172.
(46) Sun, N.-H. et al. Coupling Light into Fiber Using Second Order Fiber Bragg Gratings. In *CLEO: 2013*; Optical Society of America, San Jose, CA, 2013.
(47) Liu, V.; Fan, S. S 4: A free electromagnetic solver for layered periodic structures. *Comput. Phys. Commun.* **2012**, *183* (10), 2233−2244.
(48) Armaroli, A.; et al. Three-dimensional analysis of cylindrical microresonators based on the aperiodic Fourier modal method. *J. Opt. Soc. Am. A* **2008**, *25* (3), 667−675.

DOI: 10.1021/acsphotonics.9b01202
ACS Photonics 2019, 6, 2996−3002

(49) Lalanne, P.; et al. Light Interaction with Photonic and Plasmonic Resonances. *Laser & Photonics Reviews* **2018**, *12* (5), 1700113.
(50) Fan, S.; Joannopoulos, J. Analysis of guided resonances in photonic crystal slabs. *Phys. Rev. B: Condens. Matter Mater. Phys.* **2002**, *65* (23), 235112.
(51) Neukammer, J.; et al. Autoionization Inhibited by Internal Interferences. *Phys. Rev. Lett.* **1985**, *55* (19), 1979−1982.
(52) Sadreev, A. F.; Bulgakov, E. N.; Rotter, I. Bound states in the continuum in open quantum billiards with a variable shape. *Phys. Rev. B: Condens. Matter Mater. Phys.* **2006**, *73* (23), 235342.
(53) Lepetit, T.; Kanté, B. Controlling multipolar radiation with symmetries for electromagnetic bound states in the continuum. *Phys. Rev. B: Condens. Matter Mater. Phys.* **2014**, *90* (24), 241103.
(54) Wiersig, J. Formation of Long-Lived, Scarlike Modes near Avoided Resonance Crossings in Optical Microcavities. *Phys. Rev. Lett.* **2006**, *97* (25), 253901.
(55) Rybin, M. V.; et al. High-Q Supercavity Modes in Subwavelength Dielectric Resonators. *Phys. Rev. Lett.* **2017**, *119* (24), 243901.
(56) Taflove, A.; Hagness, S.C. *Computational electrodynamics: the finite-difference time-domain method*; Artech House, 2005
(57) Oskooi, A. F.; et al. Meep: A flexible free-software package for electromagnetic simulations by the FDTD method. *Comput. Phys. Commun.* **2010**, *181* (3), 687−702.
(58) Zhou, H.; et al. Perfect single-sided radiation and absorption without mirrors. *Optica* **2016**, *3* (10), 1079−1086.
(59) Taghizadeh, A.; Chung, I.-S. Quasi bound states in the continuum with few unit cells of photonic crystal slab. *Appl. Phys. Lett.* **2017**, *111* (3), 031114.
(60) Bogdanov, A.; Koshelev, K. L.; Kapitanova, P. V.; Rybin, M. V.; Gladyshev, S. A.; Sadrieva, Z. F.; Samusev, K. B.; Kivshar, Y. S.; Limonov, M. F. Bound states in the continuum and Fano resonances in the strong mode coupling regime. *Adv. Photon.* **2019**, *1*, No. 016001.

DOI: 10.1021/acsphotonics.9b01202
ACS Photonics 2019, 6, 2996−3002